1-1-2002

Indirect-Drive Noncryogenic Double-Shell Ignition Targets for the National Ignition Facility: Design and Analysis

Peter A. Amendt
Lawrence Livermore National Laboratory

J. D. Colvin
Lawrence Livermore National Laboratory

R. E. Tipton
Lawrence Livermore National Laboratory

D. E. Hinkel
Lawrence Livermore National Laboratory

M. J. Edwards
Lawrence Livermore National Laboratory

See next page for additional authors

Citation Details

Peter Amendt, J. D. Colvin, R. E. Tipton, D. E. Hinkel, M. J. Edwards, O. L. Landen, J. D. Ramshaw, L. J. Suter, W. S. Varnum, and R. G. Watt, "Indirect-drive noncryogenic double-shell ignition targets for the National Ignition Facility: Design and analysis," Phys. Plasmas 9, 2221 (2002)

Indirect-drive noncryogenic double-shell ignition targets for the National Ignition Facility: Design and analysis[a)]

Peter Amendt,[b)] J. D. Colvin, R. E. Tipton, D. E. Hinkel, M. J. Edwards, O. L. Landen, J. D. Ramshaw, L. J. Suter, W. S. Varnum,[c)] and R. G. Watt[d)]
University of California, Lawrence Livermore National Laboratory, Livermore, California 94551

(Received 31 October 2001; accepted 8 January 2002)

Analysis and design of indirect-drive National Ignition Facility double-shell targets with hohlraum temperatures of 200 eV and 250 eV are presented. The analysis of these targets includes the assessment of two-dimensional radiation asymmetry and nonlinear mix. Two-dimensional integrated hohlraum simulations indicate that the x-ray illumination can be adjusted to provide adequate symmetry control in hohlraums specially designed to have high laser-coupling efficiency [Suter *et al.*, Phys. Plasmas **7**, 2092 (2000)]. These simulations also reveal the need to diagnose and control localized 10–15 keV x-ray emission from the high-*Z* hohlraum wall because of strong absorption by the high-*Z* inner shell. Preliminary estimates of the degree of laser backscatter from an assortment of laser–plasma interactions suggest comparatively benign hohlraum conditions. The application of a variety of nonlinear mix models and phenomenological tools, including buoyancy-drag models, multimode simulations and fall-line optimization, indicates a possibility of achieving ignition, i.e., fusion yields greater than 1 MJ. Planned experiments on the Omega laser will test current understanding of high-energy radiation flux asymmetry and mix-induced yield degradation in double-shell targets. © *2002 American Institute of Physics.*
[DOI: 10.1063/1.1459451]

I. INTRODUCTION

Construction of the National Ignition Facility[1] (NIF) is scheduled for completion in 2009. The first ignition experiments will focus on the baseline ignition target which is a hohlraum-driven single-shell capsule consisting of a low-*Z* ablator over a DT ice layer that encapsulates deuterium–tritium (DT) gas [see Fig. 1(a)].[2] The target specifications require that the capsule be kept near the triple-point of DT (18.3° K) and the rms ice roughness be below one micron. Current techniques to control the ice roughness consist of β-layering[3] and auxiliary infrared heating.[4] The required ice smoothness has been recently demonstrated,[5] but preparing and fielding a cryogenic ignition target remains a complex procedure. In addition the baseline design requires that the capsule be driven by a four-step high-contrast (50-to-1) laser pulse-shape at 3ω (0.35 μm wavelength) with 500 TW peak power. The ignition mode is via formation of a hot spot at the capsule center and propagation of a thermonuclear burn wave to the remaining DT fuel. One-dimensional (1-D) radiation-hydrodynamics simulations predict 15 MJ of undegraded yield for a capsule driven by 150 kJ of absorbed x rays.[6]

The four principal challenges of achieving ignition with the baseline design are ensuring: (1) adequate DT ice smoothness, (2) precision shock-timing to within ± 100 ps,[7] (3) acceptable time-averaged and time-dependent low-order mode hohlraum radiation flux nonuniformity,[8] and (4) robust laser–target coupling.[9] To meet these goals an exhaustive experimental campaign, begun on the Nova laser and continuing with the University of Rochester's Omega laser,[10] has been in place. The aim of this decade-long campaign is to directly address these aforementioned technical issues, to reduce the physics uncertainties, and to maximize our confidence in achieving ignition on the NIF.

Given the complexity of cryogenic preparation, it is interesting to reconsider double-shell targets as an additional design for demonstrating and exploring ignition on the NIF. Double-shells consist of a low-*Z* ablator (outer) shell that impacts a high-*Z* (inner) shell filled with high-density DT gas at room temperature [see Figs. 1(b)–1(d)]. The outer shell acts as an efficient absorber of hohlraum-generated x rays which magnifies and transfers the acquired energy density upon spherical convergence and subsequent collision with the inner shell. Only modest velocity multiplication of the inner shell is expected according to our simulation studies. Thus, the main function of the high-*Z* inner shell is to greatly limit radiative losses from the igniting fuel and to provide added inertia for delaying fuel disassembly. The ignition mechanism for a double-shell target differs from the cryogenic single-shell case, requiring volumetric ignition of the fuel. Thus, careful shock sequencing is unnecessary because the fuel adiabat is not constrained to a low value and hence simpler laser pulse shapes may be used. A greater flexibility in pulse shape may, in turn, allow tailoring of the hohlraum plasma conditions to reduce unwanted backscatter. Additional advantages of a double-shell ignition target include (1)

[a)]Paper CI1 2, Bull. Am. Phys. Soc. **46**, 50 (2001).
[b)]Invited speaker.
[c)]Present address: Comforce Technical Services, Inc. at LANL, Los Alamos, New Mexico 87545.
[d)]Present address: University of California, Los Alamos National Laboratory, Los Alamos, New Mexico 87545.

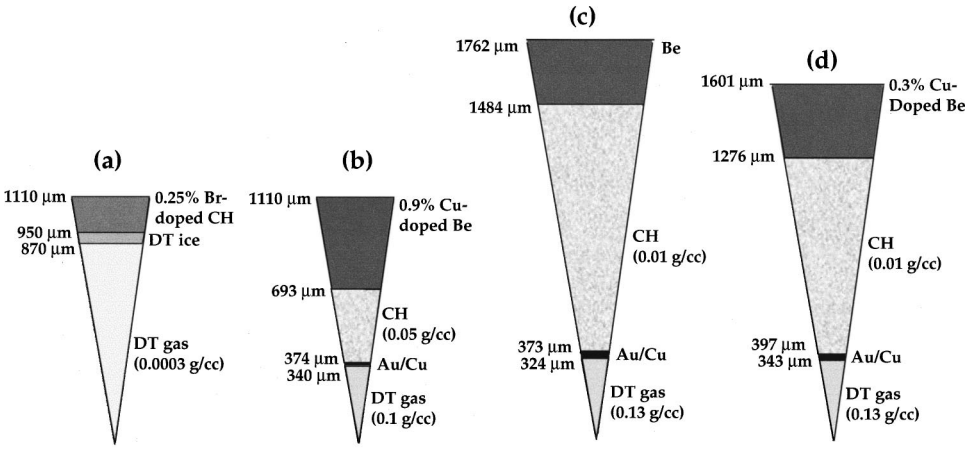

FIG. 1. Schematic diagrams of (a) NIF point-design cryogenic capsule, (b) 300 TW NIF double-shell ignition design, (c) 200 eV NIF 500 kJ double-shell ignition design, and (d) 250 eV NIF 670 kJ double-shell ignition design.

a lower peak implosion speed for ignition, (2) relaxed symmetry requirements as a result of the relatively low characteristic fuel convergence ($\approx$10), and (3) lower ignition temperatures ($\approx$4 keV) compared to hot-spot ignition ($\approx$10 keV).[11]

The concept of ignition double-shells has its origin in the 1970's when high-gain ''Apollo'' targets were explored at Lawrence Livermore National Laboratory (LLNL).[6] These cryogenic double-shell designs absorbed 800 kJ of energy and yielded 313 MJ in calculations that excluded the effects of mix. In 1979 a few double-shells were fielded on the Shiva laser but with generally low neutron yields ($<10^7$). In the 1980's it was recognized that a significant design challenge of ignition double-shell targets was controlling the highly evolved nonlinear mix on the inner surface of the high-Z shell to levels that would avoid inner-shell breakup. For this reason, LLNL abandoned double-shells as a viable path to high-gain ignition,[6] but Los Alamos National Laboratory (LANL) maintained an interest and conducted some double-shell experiments on the Nova laser in the 1990's. The LANL double-shell targets consisted of glass inner shells filled with DT gas and a plastic (CH) outer ablator. However, these targets performed poorly without exception, giving measured-over-predicted clean neutron yields (YoC) only on the order of 1%. At the time, it was conjectured that intrinsic flux asymmetry and significant laser power imbalances were responsible for the marginal performance on Nova. To test this hypothesis similar double-shell targets were shot on the Omega laser using spherical hohlraums instead of cylindrical hohlraums to provide better symmetry at the expense of less hohlraum-to-capsule coupling efficiency.[12] These targets performed as earlier with no appreciable improvement. However, a new type of double-shell target was also designed to allow x-ray imaging of the core region by thinning the glass inner shell and over-coating with CH. One-dimensional clean behavior, i.e., YoC's approaching unity, was observed for these so-called ''imaging'' double-shell capsules.[13] These implosions were repeated in cylindrical hohlraums on Omega in November 2000 and again performed well. In addition, double-shells using only pure CH were also fielded for the first time and showed similarly high YoC behavior. However, the pure glass inner-shell double-shell targets still failed to provide significant YoC performance.

One of the reasons offered for the poor performance of the standard double-shell targets to date is nonuniform preheat illumination by Au hohlraum 2–4 keV $n \geqslant 3$ ''M-shell'' line radiation.[13] While the lasers are illuminating the hohlraum wall a significant fraction of the hohlraum radiation fraction ($\approx$6%) resides in this M-shell component originating principally from the laser spots. The concern is that appreciable M-shell nonuniformity on the inner shell may seed the growth of surface perturbations that may disrupt the inner-shell integrity at late times.

An essential element for any promising NIF double-shell ignition target design is that the double-shell database with its aforementioned successes and failures be well understood. Mindful of this requirement, we build on a previous LANL double-shell ignition design[14] for the NIF by seeking an increased margin to the potentially destructive mix of high-Z pusher material into hot DT fuel. A useful figure-of-merit in this regard is the fuel-pusher fall-line which gauges the potential for mix to degrade an implosion. Very simply, a fall-line is the (straight-line) trajectory that material from the fuel–pusher interface moving at the peak implosion speed would follow toward the origin if deceleration near the end of the implosion were absent. A hypothetical limit on the spatial extent of mixed material is given by the fall-line trajectory. That is to say, the mixed material is expected to remain above the fall-line by causality. An important figure-of-merit then is the fall-line radius at peak compression. An implosion design with a fall-line radius close to the compressed radius is advantageous from the standpoint of reducing the effects of mix. There is also an important trade-off between maximizing clean yield and optimizing fall-line behavior, i.e., minimizing mix. To recover a modest amount of yield in the presence of mix requires increasing the capsule absorbed-energy. Thus, two-dimensional (2-D) integrated hohlraum simulations with LASNEX[15] are required to provide absolute design constraints on the hohlraum energetics and energy coupling efficiency to the capsule. At the same time we obtain information on hohlraum flux asymmetry control and hohlraum plasma conditions.

The main results of this paper can be summarized as

follows. In the process of optimizing double-shell fall-line behavior we find that smaller and thicker inner shells, i.e., having lower aspect ratio η, give significantly improved robustness to mix. We also obtain that constant (in time) drive-temperature profiles ($T_R = 200$ and 250 eV) rather than the constant 300 TW power case considered by LANL (giving hohlraum temperatures of nearly 300 eV) are associated with improved fall-line behavior. In addition, the laser power history required for a constant T_R is beneficial from the standpoint of minimizing the effects of plasma-mediated backscatter: peak power occurs very early in the pulse before the hohlraum has filled with ''tenth-critical density'' ($0.1n_c$) plasma. Symmetry tuning of the x-ray illumination on the double-shell capsule is required for control of the energetic x-ray (10–15 keV $n \geqslant 2$ ''L-shell'' line radiation) flux asymmetry component. Significant L-shell emission below the laser spots is preferentially absorbed by the high-Z inner shell near the pole (or hohlraum symmetry axis). Considerable displacement of the NIF inner and outer cones by nearly 1 mm is required to effect satisfactory symmetry tuning. The 2-D simulated hohlraums are found to be quite efficient compared to the standard NIF cryogenic point design, giving capsule absorbed energies as high as 30% of the input laser energy. These simulations provide justification for adopting high capsule absorbed energies in the 1-D scoping studies that result in improved fall-line behavior.

Whether the level of nonlinear mix is sufficient to thwart ignition of NIF double-shells is a key question. To this end we apply several modern mix models to gauge target robustness to short-wavelength turbulence but with the caveat that these models are phenomenological at their core. For example, we use the $K-L$ sub-grid turbulence mix modeling to estimate the amount of yield degradation from potentially destructive short-wavelength perturbations growing on the inner surface of the inner shell. For an arguably realistic set of model parameters we find that the optimized 250 eV double-shell design still ignites in contrast to the former 300 eV design. As a further check on inner-surface short-wavelength perturbation growth we apply the Ramshaw model[16] for nonlinear mixing and find robustness to mix.

Past investigations using the linear electric motor (LEM)[17] and ongoing implosion campaigns on the Omega laser have striven to constrain these model coefficients to the maximum extent. Thus, confidence in a double-shell ignition design depends critically on the ability of experiments to benchmark and validate various turbulence models beforehand. In this vein, experiments are proposed on Omega to simulate some of the features of our NIF double-shell ignition designs as a means of testing our understanding of mix.

The paper is organized as follows. In Sec. II we present some basic analysis of double-shells and introduce the 200 eV and 250 eV ignition designs based on fall-line optimization criteria. In Sec. III we describe our 2-D integrated hohlraum simulation results and the consequences for symmetry, energetics, and hohlraum plasma conditions. In Secs. IV and V we present quantitative predictions on yield degradation from mix in the intermediate- and short-wavelength regimes based on modern turbulence mix calculations. In Sec. VI we propose some campaigns on Omega to begin to address some of the outstanding issues regarding double-shell performance. We summarize in Sec. VII.

II. DOUBLE-SHELL DYNAMICS AND DESIGN

A. Dynamics

A useful starting point for understanding double-shell behavior is some simple analysis. First we address the question of optimum momentum transfer from the outer shell to the inner shell. We start with the rocket equation,

$$M_1 \frac{dv_1}{dt} = v_E \frac{dM_1}{dt}, \tag{1}$$

where M_1 is the mass of the outer shell, $v_1(<0)$ is the implosion speed, and $v_E(>0)$ is the exhaust speed. In the thin-shell approximation we can write[18]

$$M_1(t) = M_1(0) + 4\pi \int_0^t dt' r^2(t') \cdot \dot{m}(t'), \tag{2}$$

where $\dot{m}(<0)$ is the areal mass ablation rate and r is the spherical radial coordinate. Combining Eqs. (1) and (2) we find

$$v_1(t) = v_E \ln\left[1 + \frac{4\pi}{M_1(0)} \int_0^t dt' \dot{m}(t') \cdot r^2(t')\right], \tag{3}$$

where v_E is assumed constant. We next form the product of Eqs. (2) and (3) to obtain the momentum of the outer shell. Maximizing this expression for the shell momentum gives

$$\frac{4\pi}{M_1(0)} \int_0^{t_c} dt' r^2(t') \cdot \dot{m}(t') = \frac{1}{e} - 1. \tag{4}$$

Thus, maximum momentum of the outer shell is attained at t_c when nearly two-thirds of the shell has ablated away. This simple exercise provides guidance for optimizing the spacing of the two shells and is corroborated by radiation-hydrodynamics simulations of our double-shell designs (see Sec. II B).

We next address the degree of velocity multiplication imparted to the inner shell from the outer shell upon collision. If the outer shell of mass M_1 has speed v_{1i} before and v_{1f} after the collision, and if the inner shell of mass M_2 has momentum v_{2f} after the collision, then energy and momentum conservation give

$$\frac{v_{2f}}{v_{1i}} = \frac{2M_1/M_2}{1 + M_1/M_2}. \tag{5}$$

Thus, a factor-of-two velocity enhancement is possible in the limit of a large outer shell to inner shell mass ratio. For the double-shell designs that we describe in detail later the initial mass ratio is on the order of ten, but the use of Eq. (4) lowers this to nearly three at the instant of collision. Thus, a velocity enhancement of 50% is possible in the limit of no energy dissipation.

However, radiation-hydrodynamics simulations suggest that the degree of velocity multiplication for NIF double-shells is quite minimal, typically less than 10%. This feature points to the presence of significant energy dissipation at the instant of collision which we can analytically estimate. De-

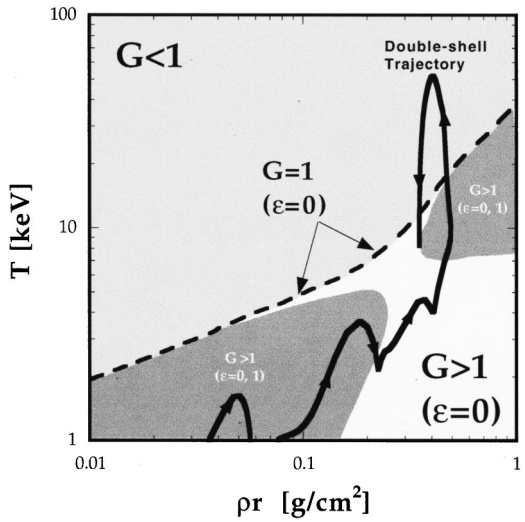

FIG. 2. Fuel energy gain (G) in areal density (ρr) and temperature (T) space for a peak implosion speed of 20 cm/μs with ($\varepsilon=1$) and without ($\varepsilon=0$) radiative losses in fuel. The central fuel trajectory for a simulated double-shell implosion is represented by a solid line. The two dark gray areas represent the only accessible regions for full radiative losses in the fuel ($\varepsilon=1$); the region of accessibility in the absence of radiative losses ($\varepsilon=0$) is indicated by the entire region below the $G=1$ (dashed) line and includes the same two dark gray regions *and* the unshaded region (lower right).

fining Q as the fraction of outer shell kinetic energy that is dissipated as heat during the shell collision, we apply energy conservation and assume $v_{1f}=v_{2f}$ to find

$$Q=\frac{1}{1+M_1/M_2}. \tag{6}$$

Thus, nearly 25% of the outer shell kinetic energy is dissipated as heat after collision for $M_1/M_2=3$.

As we remarked in the Introduction, peak implosion speeds of ignition double-shells are significantly less than cryogenic single-shell capsules which depend on hot-spot ignition. To illuminate this difference we follow Lindl[6] and invoke energy conservation at the instant of ignition onset:

$$P_w+P_\alpha+P_r+P_e$$
$$=2.3\times10^{15}\frac{\rho T(v_{\rm imp}/10^7)}{r}+8\times10^{16}\rho^2\left\langle\frac{\sigma v_{\rm imp}}{10^{-17}}\right\rangle F_\alpha$$
$$-3\times10^{16}\rho^2T^{1/2}\cdot\varepsilon-8\times10^{12}\frac{T^{7/2}}{r^2}(\mathrm{W/cm^3})=0. \tag{7}$$

Here, P_w is the rate of compressional work done on the fuel, P_α is the thermonuclear heating rate of the fuel by α-particle deposition, P_r is the rate of radiative loss from the fuel, P_e is the rate of conductive losses from the fuel, T is the temperature, ρ is the fuel density, r is the fuel radius, $\langle\theta v\rangle(\mathrm{cm^3/s})$ is the Maxwell-averaged DT cross section, F_α is the α-particle deposition fraction, and $1-\varepsilon$ is an effective albedo of the high-Z shell. One distinguishing feature of double-shell ignition is the (anticipated) reduced radiative losses from the fuel due to the high-Z shell containing the DT fuel. This is illustrated in Fig. 2 where Eq. (7) is plotted with [$\varepsilon=1$ (zero albedo)] and without [$\varepsilon=0$ (perfect albedo)] radiative losses for a peak implosion speed $v_{\rm imp}=20$ cm/μs. Also overlaid on this plot is a typical trajectory through $T-[\rho r]$ space of an ignition double-shell driven at 200 eV. Without radiative trapping, ignition is not possible at low $v_{\rm imp}$ because of the clear inaccessibility of the high temperature and high areal density domain. This scenario is representative of a low-Z (cryogenic) pusher where radiative equilibrium in the fuel is not established. By contrast the high-Z pusher of a double-shell traps the radiation in the fuel and promotes radiative equilibrium with the inner surface of the pusher. As shown in Fig. 2, the double-shell trajectory traverses both of the $\varepsilon=1$ (shaded) regions to ignite at a temperature of several keV and an areal density of 0.4 g/cm^2. At higher implosion speeds, e.g., $v_{\rm imp}=30$ cm/μs, the shaded $\varepsilon=1$ regions coalesce to allow ignition of a cryogenic single-shell capsule [Fig. 1(a)].[6]

B. 1-D double-shell designs

Our starting point is the 1-D ignition design of Harris and Varnum[14] as shown in Fig. 1(b). This design requires 300 TW of laser power delivered over 6 ns to give a hohlraum temperature T_R of nearly 300 eV and a capsule yield of nearly 2.4 MJ. Here we pursue an alternative design approach which emphasizes robustness to deleterious mixing of high-Z pusher material into hot DT fuel. The figure-of-merit we will use is a so-called ''fall-line'' of the implosion trajectory of the fuel–pusher interface. The idea of a fall-line analysis is as follows. The contamination of the fuel is causally limited to the extent that high-Z material cannot overtake the position the interface would have if it continued to move inward to the origin ($r=0$) at its peak velocity. The tangent line to the interface trajectory at the time of deceleration onset, i.e., peak $v_{\rm imp}$, defines a fall-line which will intercept $r=0$ at some later time. In order to minimize the effects of mix the target design is adjusted so that the fall-line intercept the origin after peak burn by as much of a time margin as possible. Forming the difference between the time of peak burn and the time at which the fall-line reaches the origin, normalized to the full-width half-maximum (FWHM) burn-width, defines a fall-line delay parameter $\Delta\tau$. Our philosophy is to keep $\Delta\tau$ as negative as possible, even at the expense of a significant reduction in the clean yield. The goal is the demonstration of thermonuclear ignition—not high gain—which requires aggressive mitigation of damaging mix.

The direction we choose to pursue for minimizing $\Delta\tau$ is through use of constant hohlraum drive-temperatures and higher capsule absorbed energies. A constant T_R is beneficial from the standpoint of requesting peak laser power very early in time before the hohlraum gas-fill density has increased appreciably due to high-Z plasma wall blow-off. In addition, damage initiation of the laser glass may be reduced with the use of such a pulse-shape (see Sec. III A), thereby making available more laser energy. We will explore hohlraum drive temperatures of 200 eV and 250 eV, the former being easily accessible on the Omega laser for experimental scoping studies. Improved fall-line behavior is also correlated with increased capsule absorbed energy as we now show analytically. Applying energy conservation to the fuel and pusher as the fuel is adiabatically compressed gives for the pusher velocity,

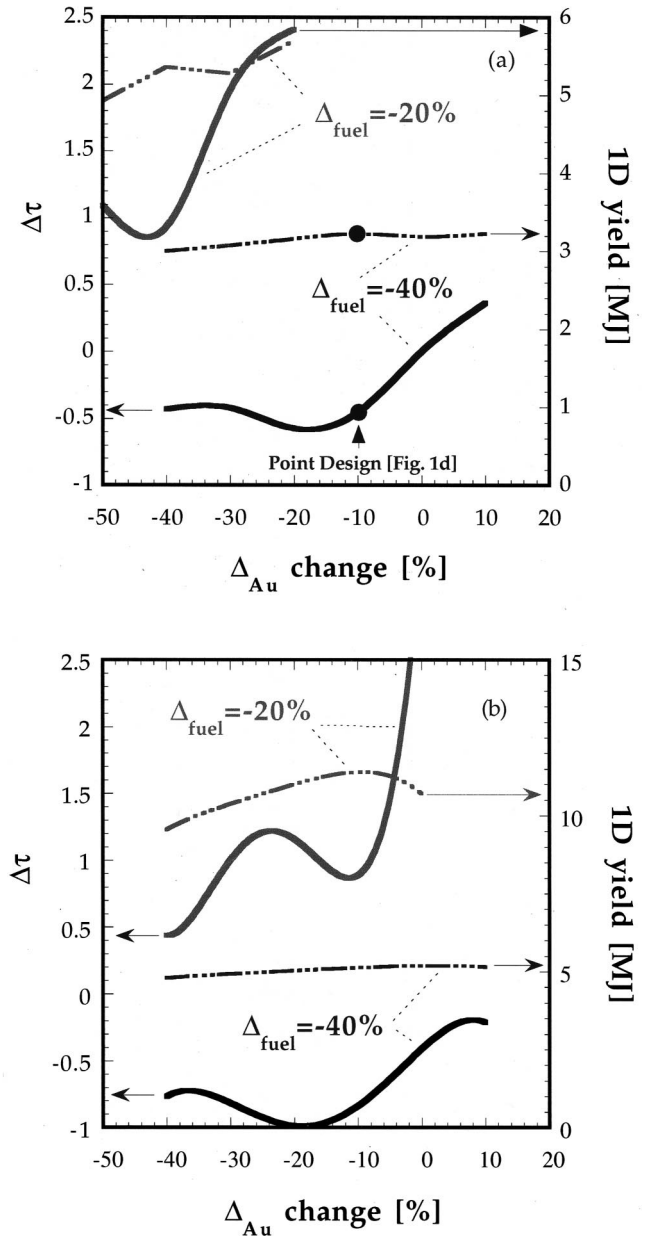

FIG. 3. Normalized fall-line parameter $\Delta\tau$ and simulated one-dimensional yield versus changes in inner-shell thickness Δ_{Au} and fuel radii Δ_{fuel} driven at 200 eV for (a) a 500 kJ design and (b) a 750 kJ design. Indicated changes are relative to the former design [Fig. 1(b)] scaled in dimension by (a) $4^{1/3}$ and (b) $6^{1/3}$.

$$v_2(r) = -v_{\text{imp}}\sqrt{1-\frac{1}{\beta}\left(\frac{r_0^2}{r^2}-1\right)}, \tag{8}$$

where v_{imp} is the pusher velocity at the instant of deceleration onset t_0, and r_0 is the radius of the fuel–pusher interface at t_0. Here, the parameter β is defined as

$$\beta = \frac{M_2 v_{\text{imp}}^2}{4\pi P_s r_f^3}\left(\frac{r_0}{r_f}\right)^2 = \left(\frac{r_0}{r_f}\right)^2 - 1, \tag{9}$$

where P_s is the fuel stagnation pressure and r_f is the minimum radius attained by the fuel at t_f. The time $\delta t = t_f - t_0$ required to reach stagnation ($v_2 = 0$) is obtained from integrating Eq. (8):

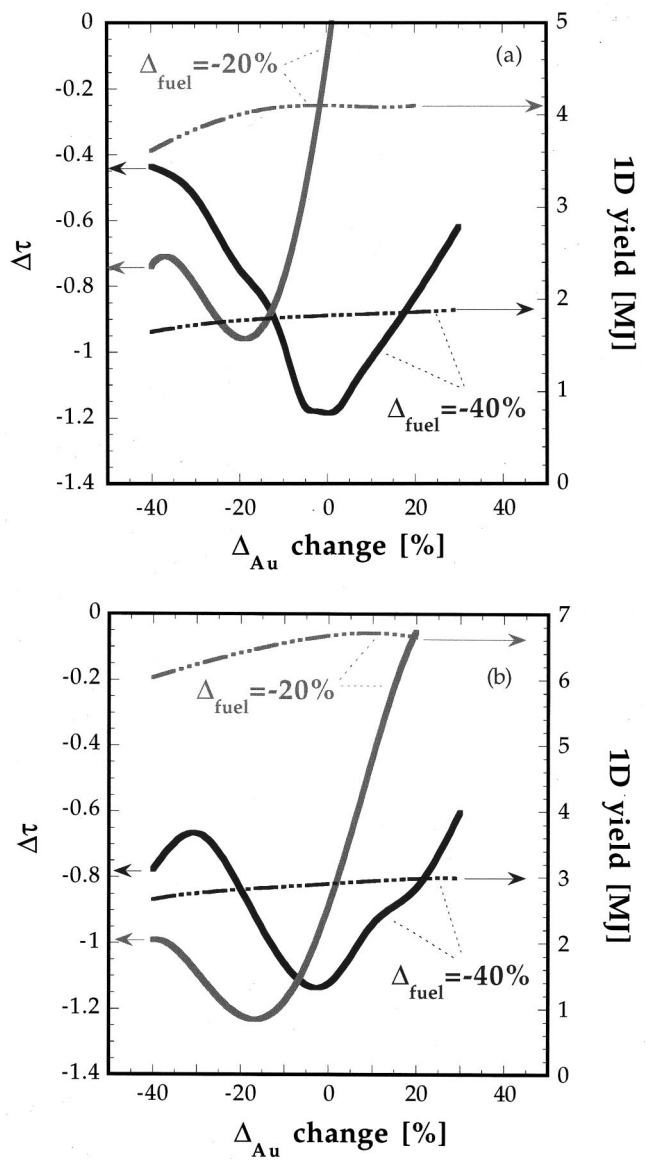

FIG. 4. Normalized fall-line parameter $\Delta\tau$ and simulated one-dimensional yield versus changes in inner-shell thickness Δ_{Au} and fuel radii Δ_{fuel} driven at 250 eV for (a) 500 kJ design and (b) 750 kJ design driven. Indicated changes are relative to the former design [Fig. 1(b)] scaled in dimension by (a) $(2.25)^{1/3}$ and (b) $(3.4)^{1/3}$.

$$\delta t = \frac{r_0}{v_{\text{imp}}}\cdot\frac{\beta}{1+\beta}. \tag{10}$$

A useful metric of fall-line behavior is the difference of r_0 and the fall-line radius at t_f normalized to r_0: $(r_f/r_0)\cdot\beta/(1+\beta)$. Thus, good fall-line behavior is associated with small values of β. From Eq. (9) a trajectory of the fuel–pusher interface that can reach peak implosion speed v_{imp} just before fuel stagnation will minimize β and ensure favorable fall-line behavior. This condition of reaching v_{imp} at higher fuel pressure can be met most directly by accessing higher capsule absorbed energies.

We now develop some scaling law relations to explore designs with different capsule absorbed energies. Let the parameter s denote the capsule absorbed energy. For the constant drive conditions of interest the flux remains constant so

that $r^2 t \propto s$. From Eq. (4) with $\dot{m} \approx T_R^3$ and $M_1 \propto r^3$, we have $r \propto t$. We thus obtain the following scaling relations:

$$r \to r \cdot s^{1/3}, \quad t \to t \cdot s^{1/3}, \quad v \to v, \quad P \to P \cdot s^{2/3}, \tag{11}$$

where P is the power.

Our 500 kJ 200 eV double-shell design is shown in Fig. 1(c). Aside from the overall 60% larger scale of this target compared to the 350 kJ former target [Fig. 1(b)], we emphasize some important design differences. First, the (inner) shell aspect-ratio η is considerably smaller than in the former design for two reasons: (1) to facilitate target fabrication with respect to containment of the high fuel fill, and (2) to reduce feed-through [$\approx \exp(-l/\eta)$] of outer surface perturbations with Legendre mode number l. Second, we have dispensed with Cu-dopant in the beryllium ablator in order to maintain a high mass-ablation rate and keep the peak implosion velocity above the critical value of 19 cm/μs. Third, we increased the DT fuel fill by 30% to provide more yield margin. The design strategy was to vary the ablator thickness for a given inner shell thickness and radius until optimal fall-line behavior was achieved. Figures 3(a) and 3(b) illustrate the result of this procedure for capsule absorbed energies of 500 kJ and 750 kJ. The tradeoff between acceptable fall-line behavior and yield is very evident: nearly a factor-of-two in thermonuclear yield is sacrificed in order to accommodate negative values of $\Delta\tau$. Another feature of note is that the fall-line behavior for the 750 kJ case [Fig. 3(b)] is significantly improved—in addition to a near factor-of-two improvement in yield.

The 670 kJ 250 eV design is schematically shown in Fig. 1(d). Again, the distinguishing features of this target are the markedly lower aspect-ratio inner shell, the reduced Cu-dopant concentration in the outer shell (0.3 at.%) compared to the former design [Fig. 1(b)], the modestly higher fuel fill, and the larger ratio of shell radii ($\approx$3). The clean yield for this target is 4.1 MJ and $\Delta\tau \approx -1$. The relatively thicker and smaller inner shell in this design is intended to provide improved fall-line behavior. Figures 4(a) and 4(b) show the yield and fall-line behavior for very similar capsules at 500 kJ and 750 kJ of absorbed energy. A main distinction with Figs. 3(a) and 3(b) is the relative robustness of larger inner-shell designs driven at 250 eV. We now see that the $\Delta_{\text{fuel}} = -20\%$ design has far more favorable fall-line behavior than the corresponding 200 eV versions. This feature allows access to a higher yield while controlling the potential for damaging mix. A caveat is that the improvement in fall-line behavior comes at the expense of relatively higher aspect-ratio inner-shells which may promote stronger feed-through of perturbations. Comparing the $\Delta_{\text{fuel}} = -40\%$ targets in the 200 eV and 250 eV designs shows overall that the higher drive case is characterized by modestly better fall-line behavior but somewhat lower yields. To regain the higher yields while maintaining good fall-line behavior in the 250 eV case may require stronger consideration of the $\Delta_{\text{fuel}} = -20\%$ targets.

We have not looked at 300 eV versions of the above double-shell targets to date. However, the laser power requirements and the higher risk of damage initiation to the laser glass slabs will not likely make this type of target an attractive double-shell option for the NIF.

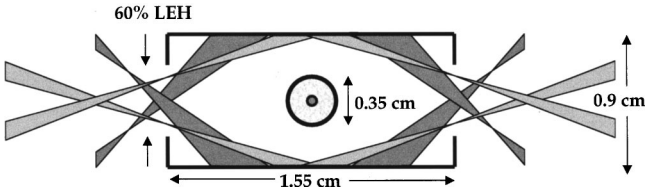

FIG. 5. Schematic of hohlraum geometry for 200 eV 500 kJ double-shell design [Fig. 1(c)].

III. ENERGETICS AND SYMMETRY

Having shown the merit of high capsule absorbed energy for achieving double-shell ignition, we turn to the practicality of fielding such targets in a NIF hohlraum. To address this question, we must perform 2-D integrated hohlraum simulations for assessing the energetic requirements and tuning the flux asymmetry to acceptable levels for ignition.

A. 2-D analysis of 200 eV hohlraum

A 200 eV hohlraum enclosing the previously described 500 kJ double-shell capsule is shown schematically in Fig. 5. Two cones of rays from each side are incident on the interior of a hohlraum made from a ''cocktail'' mixture of high-Z elements (26% U, 18% Pb, 18% Ta, 19% Dy, 19% Nd) for reducing Marshak wave wall losses and thereby improving laser–target coupling.[9] The laser-entrance-holes (LEHs) are 60% of the hohlraum diameter and the hohlraum is filled with a 1 mg/cm^3 equimolar mixture of He–H to aid in symmetry control. Use of time-varying power ratios between the outer and inner cones to improve symmetry, i.e., beam phasing, is not invoked. The laser power history is shown in Fig. 6 and corresponds to 1.6 MJ of laser energy. Note that the hohlraum is calculated to be quite efficient by current standards, exceeding 30%. Further improvement in target coupling is possible with the use of even smaller LEHs due to the relatively large scale of the hohlraum (''scale'' 1.6) under consideration and the fixed spot size of the rays at best focus

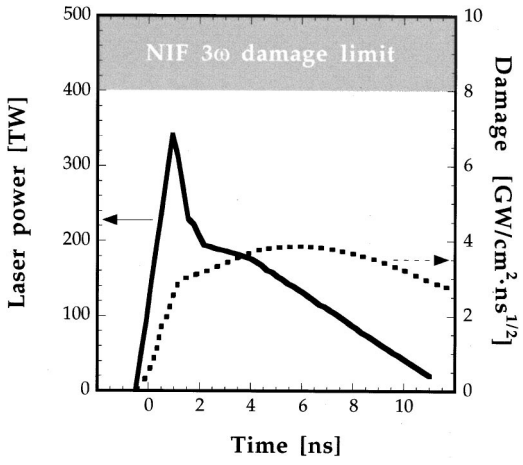

FIG. 6. Simulated laser power (bold) and damage (dashed) history for a 200 eV hohlraum (Fig. 5) driving a 500 kJ double-shell target [Fig. 1(c)].

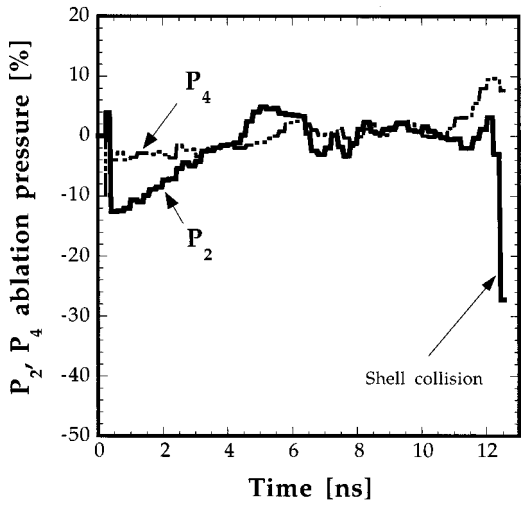

FIG. 7. Normalized second- and fourth-Legendre coefficient of the ablation pressure asymmetry history on the outer shell of the 200 eV 500 kJ double-shell target.

($\approx$250 μm radius). A polyimide window for containing the hohlraum gas-fill has not been included in this first generation simulation study but is not expected to significantly affect our conclusions.

A key constraint on any NIF power profile is the initiation of damage to the final optics assembly from localized absorption and heating of blue laser light near glass surface imperfections. The damage integral takes the form[9]

$$\text{Damage} = 1.1 \times \int_0^t \frac{I(s)}{\sqrt{t-s}}\, ds, \tag{12}$$

where I is the laser intensity (GW/cm^2), t and s are in nanoseconds, and the coefficient of 1.1 normalizes the damage to a 3 ns Gaussian-equivalent pulse-shape as a convenient metric of comparison. Figure 6 shows also the laser glass damage-initiation integral for the accompanying 3ω pulse-shape. From a damage threshold standpoint the 200 eV drive laser pulse-shape is rather benign, giving less than half the indicated NIF damage specification and allowing the prospect for even higher energy on target.

We have succeeded in obtaining ignition of our 200 eV 500 kJ double-shell target according to integrated hohlraum simulations. The thermonuclear yield is almost 2 MJ which compares favorably with the 1-D yield of 3.2 MJ. The symmetry of the implosion is not ideal and tends towards "pancaking," i.e., the second Legendre coefficient of the imploded fuel–pusher interface is negative. Figure 7 shows the second- and fourth-Legendre coefficient of ablation pressure asymmetry for the outer shell versus time; higher resolvable even-mode radiation asymmetries ($l=6,8$) do not have a significant effect according to the simulations. Figure 7 verifies that the outer-shell lower mode ($l=2,4$) ablation pressure asymmetry is remarkably good up to the time of shell collision with the time-integrated ablation pressure asymmetry less than 2% for both P_2 and P_4. However, a different situation for the inner-shell ablation pressure asymmetry is seen in the simulations. The time-integrated ablation pressure asymmetry up to the time of shell interaction is nearly 12% for P_2 and 17% for P_4, both of which add in concert to cause a pancaked implosion and abbreviated thermonuclear burn. Ordinarily, such a large level of flux asymmetry would preclude ignition. The exception in our case is because the ablation pressure on the inner shell is only 2–3% of the outer shell ablation pressure before shell collision. However, this level of asymmetry is still sufficient to modestly degrade the yield.

On closer inspection of this source of flux asymmetry on the inner shell, one finds that a significant fraction ($\approx$10%) of the radiation density in the volume between the two shells resides in high-energy x rays, i.e., 8–15 keV. The source of this L-shell radiation seen in the simulations is the high-Z hohlraum blow-off material intercepting the laser rays near the LEHs. In order to satisfactorily tune away this L-shell flux asymmetry component both inner and outer cones were displaced inward by over a millimeter compared to the baseline cryogenic hohlraum designs. The thermal x-ray component ($<$1 keV) of flux asymmetry on the outer shell remains tolerably small under such large cone translations because of the low shell convergence (3–4) and high hohlraum efficiency. An efficient hohlraum has a high wall albedo to thermal x rays which acts to reduce the cone-to-wall contrast of x-ray emissivity and thereby lower the sensitivity to laser pointing. However, L-shell x-ray asymmetry remains very sensitive to laser pointing because of the highly localized source for these x rays. In addition to displacing the laser cones for L-shell symmetry control, the use of higher gas densities in the hohlraum and implementing beam phasing between the outer and inner cones could also be exploited.

We have also started to consider the effect of plasma-mediated laser backscatter in the 200 eV hohlraum with the aid of the Laser–plasma Interaction Postprocessor[19] (LIP). LIP uses the flow speeds, temperatures, and densities along a laser raypath calculated by a radiation-hydrodynamics code to analyze the steady state, kinetic linear growth-factors of stimulated Brillouin backscatter (SBS) and stimulated Raman backscatter (SRS). We initially ran LIP on our 200 eV hohlraum design where the inner cone foci were situated 0.2 cm inside the LEH. Large SBS growth was found to occur in the He–H gas in the vicinity of the LEH. To ameliorate this SBS growth we moved the inner cone foci to a position 0.2 cm outside the LEH and found lower growth rates for backscatter because the light intensity is less. According to LIP the linear SBS gain exponent has a maximum value of $\approx$18 near peak laser power, which nearly matches the value predicted[6] for the inner-cone on the NIF point-design at peak power ($\approx$20). For both hohlraums most of the gain occurs in the low-Z gas, although well inside the LEH for the case of the point-design. Much of the inner cone SBS found in the 200 eV design is due to the relatively low temperature ($\approx$3 keV) of the gas near the LEH (lower than in the point design) and the relatively higher electron density ($n_e/n_c \approx 0.04$, as compared to $n_e/n_c \approx 0.02$ for the point design). These parameters are offset by a relatively low intensity ($<10^{15}$ W/cm^2). In the outer cones the peak SBS is calculated to reach only $\approx$13 gain exponents compared to nearly 18 for the point design.

We have calculated SRS levels for the inner cone on the

200 eV design. The peak SRS gain exponent is only ≈12, well below the predicted value of nearly 22 for the point design.[6] This change in the gain exponent primarily arises from the reduction in intensity between the LEH and the wall. For the outer cone SRS gain exponents of only ≈7 are approached compared to ≈10 for the point design. Overall, the indicated Raman backscatter in our 200 eV hohlraum design appears to be manageable with the flexibility for further reduction as needed.

We have also estimated the degree of ponderomotive filamentation within the two cones. A useful figure-of-merit is as follows: $Q=I(\mathrm{W/cm^2})\cdot\lambda^2(\mu\mathrm{m})\cdot(n_e/n_c)\cdot[3/T_e\ \mathrm{keV}]\cdot(f/8)^2$, where λ is the laser wavelength. When Q is less than the critical value of 10^{13} W for a NIF $f/8$ KPP-smoothed beam the filamentation instability is weak and little beam spraying can be expected. Corresponding to this critical value of Q is the filamentation gain per laser speckle $G_s=0.5$.[20] We find that the inner (outer) cone has at most $G_s=0.3$ (0.2), indicating that filamentation should be controllable.

B. Integrated hohlraum analysis of 250 eV design

We carry through the same analysis for the 250 eV double-shell target design [Fig. 1(d)]. The hohlraum used to drive this 670 kJ target is about $(4/3)^{1/3}$ times smaller in dimension than the 200 eV hohlraum driving our 500 kJ target (Fig. 5). The required laser power history and associated damage integral are similar to Fig. 6 but with a peak power of 575 TW and maximum damage initiation of 6.5 J/cm^2. The total laser energy is 2.5 MJ but the NIF damage limit is still comfortably avoided. With this damage margin the requested energy at 3ω appears possible despite being higher than the nominal 1.8 MJ. A NIF 2ω option would provide a higher damage margin and allow even higher laser energies.[9] To relax further the laser requirements a longer risetime of the laser pulse-shape could be implemented without jeopardizing the ignition design. The resulting lower intensity translates into lower levels of plasma-mediated backscatter.

The target yield from this 2-D simulation is 2.8 MJ which compares favorably with the 1-D yield of 4.1 MJ. Again, flux asymmetry is responsible for the degradation as in the case of the 200 eV design. The calculated ablation pressure asymmetry on the outer shell is benign as before; cf. Fig. 7. We also find that the time-integrated ablation pressure asymmetry on the inner shell up to the instant of shell collision is considerably improved over the 200 eV design, giving $P_2\approx 5\%$, $P_4\approx 1\%$. However, this three-fold reduction in percent asymmetry is nullified by a three-fold increase in the level of 10–15 keV flux reaching the inner shell for the 250 eV hohlraum, making inner capsules in both hohlraums equally sensitive to L-shell flux asymmetries. Increasing the Cu-dopant in the Be outer shell for either target would reduce the flux reaching the inner surface, but not without incurring a significant penalty in the mass ablation rate. Higher mode radiation asymmetries ($l=6,8$) appear to be tolerably low for this hohlraum because of robust radiation transport smoothing[8] ($\approx l^{-2.5}$) and the large ratio of hohlraum radius to inner shell radius (≈20).

As in the 200 eV design, a further improvement in tuning lowest-order mode asymmetry is required. Although the yield degradation in the designs is only about 30% from flux asymmetry alone, higher-mode perturbations such as from feed-through can be superimposed on the low-order distortions to the point of thwarting ignition altogether. For this reason symmetry optimization is an essential component of overall mix control. Beyond the $l=2-8$ even modes considered in this section, tolerances to low-order odd modes arising from target imperfections, e.g., shell nonconcentricity ($l=1$) and laser power imbalances, must also be established.

IV. INTERMEDIATE-WAVELENGTH PERTURBATIONS

An important concern for double-shell stability is the feed-through of outer-surface perturbations on the inner shell to the inner surface. At the time of shell collision, an impulsive-like acceleration will be delivered to the outer surface of the inner shell promoting Richtmyer–Meshkov instability (RM). Subsequent shocks propagating across this interface will transmit the amplified perturbations to the inner surface according to the feed-through expression:[6] $\mathrm{FT}=\exp(-l/\eta)$. Therefore, shells with a large aspect-ratio η promote the largest instability growth and possible shell disruption. We can analytically estimate the most dangerous mode number and its growth as follows. The Rayleigh–Taylor (RT) growth factor for an inner surface perturbation at deceleration onset scales as $\approx\exp(\sqrt{2l})$, where the conduction scale-length is ignored and the deceleration distance is taken to be the final fuel radius. Forming the product of this growth-factor and the feed-through factor above, and then solving for the maximum growth factor GF, gives

$$\mathrm{GF}\approx e^{\eta/2},\quad \text{at } l=\eta^2/2. \tag{13}$$

Thus, with $\eta\approx 6-7$ for our two double-shell target designs, maximum growth occurs for $l\approx 20-25$. This range of mode numbers is amenable to direct numerical simulation (DNS) which we have performed with CALE[21] using a measured glass surface power spectrum (as a surrogate for Au) to initialize the perturbations (see Fig. 10 below). Figure 8 shows the fuel–pusher interface and ion temperature contours 150 ps *after* peak burn for the 250 eV design [Fig. 1(d)] using $l_{\max}=32$. Simulations with a higher mode-number cutoff ($l_{\max}=96$) show very similar results with a yield degradation of only several percent. At the instant of peak burn the perturbations are barely perceptible which is attributable to the optimized fall-line behavior, low aspect-ratio inner shell, and realistically smooth surface spectrum.

V. SHORT-WAVELENGTH PERTURBATIONS

Until now we have considered resolvable perturbations and their calculable effect on target performance. Unfortunately, we are not currently able to make DNS predictions much beyond $l=100$, and we resort to phenomenological methods for estimating the contribution to mix from unresolved short-wavelength modes. In the absence of ablative and density-gradient scale length stabilization, the short-

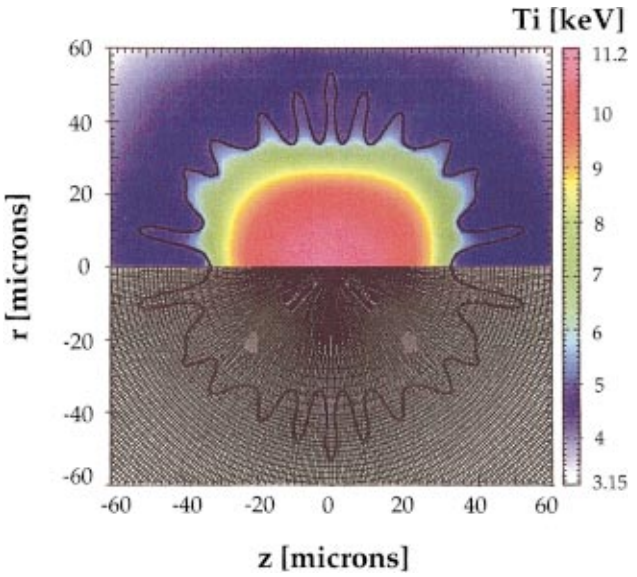

FIG. 8. (Color) Simulated ion temperatures (upper frame) and zoning mesh (lower frame) for 250 eV 670 kJ double-shell target +150 ps after peak thermonuclear burn using the surface spectrum from Fig. 10. Heavy black line marks the location of the simulated fuel–pusher interface.

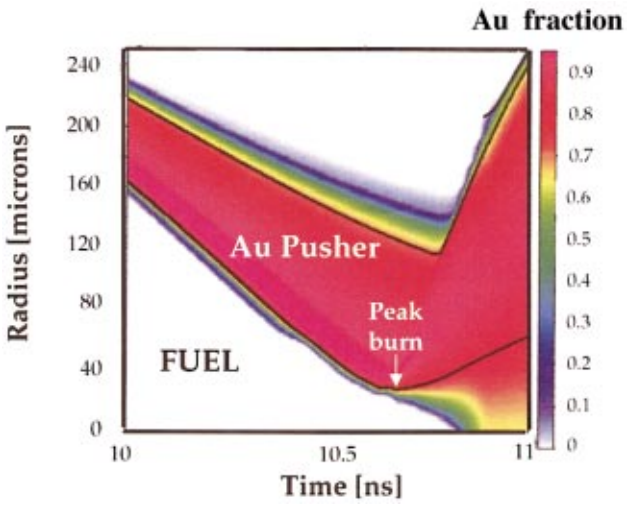

FIG. 9. (Color) The simulated mix fraction of Au versus time with an overlaid fuel–pusher interface using CALE with a K–L mix model for the 250 eV 670 kJ double-shell target.

wavelength modes will nonlinearly saturate after reaching an amplitude on the order of their wavelength and then proceed to feed energy into lower modes via strong mode-coupling. Thus, the peak of the accumulating perturbation energy spectrum will shift to ever increasing wavelengths eventually culminating in a fully evolved mixing layer where all memory of the initial conditions becomes lost (as in the case of RT instability).[22] A full spectrum of modes is required to describe this process deterministically, but the computational requirements are generally prohibitive for the relevant regime of large Reynolds number ($\mathrm{Re}>1000$). The spectrum of growing modes is bounded above by those modes that are viscously damped: $l>2\pi\cdot \mathrm{Re}\simeq 10^4$. For ignition double-shells the largest allowed mode numbers correspond to wavelengths on the order of tens of nanometers which is presently inaccessible by DNS. In addition, the dissipation of energy for large Re occurs over small spatial scales or ''eddies'' ($\approx r_f\cdot \mathrm{Re}^{-3/4}$) with characteristic size on the order of a hundred nanometers or less for ignition double-shells. Describing such small-scale turbulence structure *ab initio* with DNS techniques is also not currently practical and we turn to phenomenological methods.

A. $K-L$ turbulence modeling

The $K-L$ sub-grid turbulence mix model in CALE has been exercised for our 250 eV double-shell design [Fig. 1(d)]. Here, K refers to the turbulent or eddy kinetic energy per mass that resides in modes which are computationally unresolved and have not yet thermalized or dissipated their kinetic energy into heat. K can be defined in this manner even when the system has not reached a statistical steady state normally referred to as turbulence. The second parameter of the model L is the eddy scale length which is used in place of the more familiar parameter:[23] $\varepsilon=C_D K^{3/2}/L$ where C_D is the bubble drag coefficient. The $K-L$ representation is more convenient from the standpoint of specifying and remembering initial conditions, i.e., initial surface finish, which are essential for properly describing the RM instability. The $K-L$ equations comprise a system of coupled nonlinear partial differential equations to which must be added the diffusion equations for species concentration and energy. This system of equations is then solved in conjunction with a standard hydro code, e.g., CALE, to assess the evolution of mix and its effect on target performance. Figure 9 shows the fuel–pusher interface trajectory and the intrusion of high-Z Au into the fuel volume after a minimum radius is reached for our 250 eV design. According to this simulation our double-shell target ignites to produce over 1 MJ of the yield; by contrast, the former design [Fig. 1(b)] fails to ignite. The difference is a direct result of the improved fall-line behavior and of reduced perturbation feed-through. We must emphasize that the $K-L$ model is phenomenological at its core, and, as such, relies on a suite of parameters for implementation. Although our adopted set of modeling parameters arguably enjoys experimental support, other choices not compatible with ignition are also possible. Ongoing experiments on the Omega laser and a past analysis of LEM data are currently being used to further constrain these parameters and improve the predictive capability of the $K-L$ mix model.

B. Ramshaw nonlinear mix model

Another model for describing the evolution of small-scale mix is due to Ramshaw.[16] This model obtains a second-order ordinary differential equation for the mix width h across a fluid interface for an arbitrary acceleration history $a(t)$:

$$\dot{\lambda}\cdot\ddot{h}+\tfrac{1}{2}\dot{\lambda}\cdot\dot{h}+2\pi c|\dot{h}|\dot{h}-2\pi A a h=0, \tag{14}$$

where λ is the perturbation wavelength, overdots denote differentiation, $A=(\rho_2-\rho_1)/(\rho_1+\rho_1)$ is the Atwood number, ρ_1 and ρ_2 are the densities of the adjacent fluids, and is a c constant constrained by the asymptotic behavior of the RT

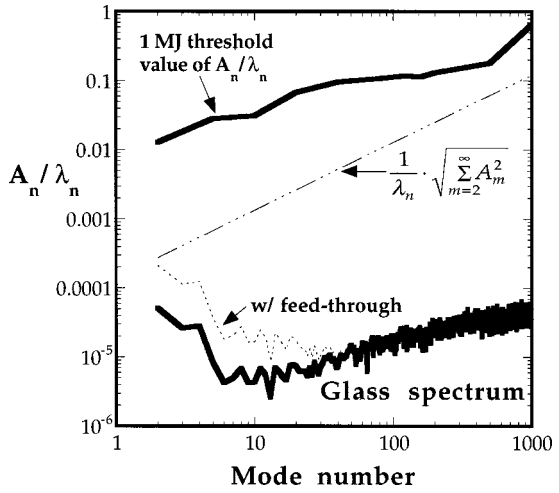

FIG. 10. The ratio of the amplitude to wavelength versus the Legendre mode number for a measured glass spectrum (lower curve), measured glass spectrum with calculated feed-through amplification (dotted line), a rms glass spectrum including feed-through (dot–dashed line), and a calculated 1 MJ threshold value based on the Ramshaw mix model (upper curve) applied to the 250 eV 670 kJ double-shell target design.

and RM instabilities. Equation (14) reproduces the known linear and nonlinear behavior for the RT and RM instabilities. Further work has generalized Eq. (14) to include the effects of shear and compression.[24] The Ramshaw model has been recently implemented in LASNEX for mix studies. Figure 10 shows the results of the Ramshaw model applied to our 250 eV double-shell design. The fundamental input quantity is the ratio of initial perturbation amplitude A_l to the perturbation wavelength λ_l. Figure 10 provides the maximum initial value of A_l/λ_l vs l that the inner surface of the capsule can tolerate while still providing a yield of 1 MJ (top curve). As a basis of comparison we include a measured glass surface spectrum (bottom curve). Clearly, a large margin of initial perturbation amplitude is allowed according to this simple model. However, the Ramshaw model does not include perturbation feed-through and explicit mode-coupling in the presence of a full spectrum of modes which may erase much of the indicated margin.

The effect of perturbation feed-through can be estimated as follows. Upon shell collision an outer surface perturbation on the inner shell will grow according to the (ideal) RM growth-rate: $A_n(t)=A_n(0)\cdot k_n\cdot \Delta r$, where k_n is the perturbation wavenumber and Δr is the distance the interface has traveled before a second shock arrives to propagate the amplified perturbation to the inner surface (see Sec. IV). The feed-through factor is nearly exponential for $l>10$, i.e., FT $\approx \exp(-l/\eta)$, but spherical effects become important at smaller values of l, requiring the following modification: $\mathrm{FT}\approx 1/[(1+1/\eta)^{l}-(1+1/\eta)^{-l-1}]$. We form the product of the above RM growth-rate and the feed-through factor, taking Δr as the radius of the shell for an upper-limit, and apply the result to the surface spectrum in Fig. 10 as shown (dotted line).

A possible upper limit for gauging the effect of a full spectrum of perturbations is conjectured by collapsing all of the initial perturbation amplitude, including feed-through, into a single mode and then initializing the Ramshaw model with use of this elevated amplitude. Figure 10 shows the result of this procedure and the remaining margin for achieving 1 MJ yield (dot–dashed line). Over the entire range of mode numbers shown the Ramshaw mix model suggests that ignition of the 250 eV double-shell target is possible. The caveat for this analysis is again the underlying phenomenological basis of the model through a reliance on a set of parameters that require experimental validation.

C. Fall-line analysis

We have gone to considerable length to optimize fall-line behavior as a necessary condition for target robustness. In this section we quantify the effect of a given fall-line delay on target performance in terms of a phenomenological penetration fraction γ.

For RT dominated perturbation growth (as in ignition double-shells) the fall-line analysis can be shown to have an intuitively close connection with nonlinear RT behavior. Youngs has shown that a similarity solution with length scale proportional to gt^2 describes the late time evolution of the mixing layer where g is the acceleration of the interface.[22] Subsequent studies have established that the mix width evolution in the nonlinear regime can be well described by the relation

$$h_i=\alpha_i A g\cdot(t-t_0)^2, \tag{15}$$

where $i=1,2$ labels the fluid being penetrated, α_1 (α_2) is the growth coefficient for spikes (bubbles), and $\alpha_1>\alpha_2$. Experiments show that α_2 is relatively insensitive to Atwood number, assuming values in the range: 0.04–0.07.[17] Spike penetration of the fuel on the other hand shows more variation with A: $\alpha_1\simeq\alpha_2\cdot(1+A)$ for $A<0.8$. Equation (15) can be related to a fall-line analysis. Near minimum volume of the imploding fuel the trajectory of the fuel–pusher interface can be approximated as

$$r(t)\cong L-v_{\mathrm{imp}}\cdot(t-t_0)+\frac{v_{\mathrm{imp}}\cdot(t-t_0)^2}{2(t_f-t_0)}. \tag{16}$$

Forming the difference between Eq. (16) and the fall-line trajectory $r_{\mathrm{fall}}=L-v_{\mathrm{imp}}(t-t_0)$ gives for the fall-line difference Δr_{fall},

$$\Delta r_{\mathrm{fall}}(t)=\frac{v_{\mathrm{imp}}(t-t_0)^2}{2(t_f-t_0)}. \tag{17}$$

Comparing Eqs. (15) and (17) suggests the natural introduction of a time-independent penetration fraction γ of the fuel by pusher material. That is to say, we have established a theoretical basis for representing the spatial evolution of fuel–pusher mixing in terms of a (constant) fraction of the distance between the interface and the fall-line. In reality, the presence of RM instability and a time-varying Atwood number will complicate this simple picture somewhat, but the property of a one-parameter (γ) description of the mix process is nonetheless appealing.

We have analyzed the 250 eV double-shell design for yield performance versus fall-line penetration fraction γ. Figure 11 offers a comparison of this design with the former

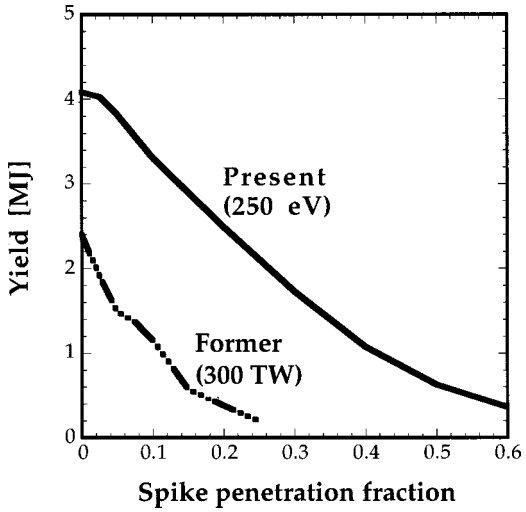

FIG. 11. The one-dimensional simulated yield versus the spike penetration fraction for a 250 eV 670 kJ design (solid line) and former 300 TW design (dot–dashed line) [Fig. 1(b)].

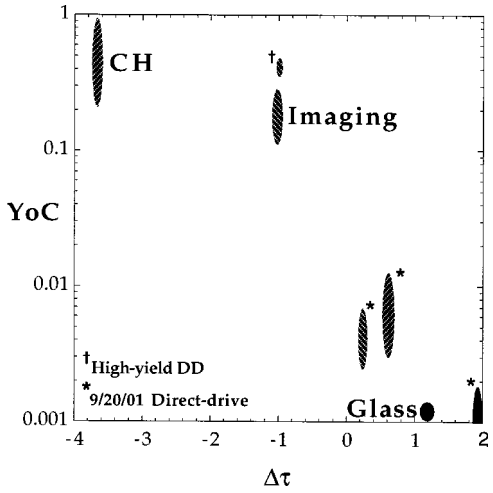

FIG. 12. The measured neutron yield over the simulated clean (no mix) yield versus normalized fall-line parameter $\Delta\tau$ for indicated Omega LANL directly-driven and cylindrical hohlraum-driven targets. CH targets are pure plastic inner and outer shell double-shells filled with DD; glass targets have a pure glass inner shell with 1.8% Br-doped CH outer shell and DT fill; imaging targets have a glass inner shell overcoated with CH and undoped outer CH shell; a high-yield version of the imaging targets has higher DD fuel fill and thinner outer shell.

design [Fig. 1(b)], showing significantly more tolerance to high-Z pusher penetration of the fuel. We find that the 250 eV design can tolerate as much as a 40% spike penetration fraction and still give over 1 MJ of yield. The increased margin is a result of more energy absorbed by the capsule and improved fall-line behavior as evidenced in Fig. 11 by the slower decrease in yield with an increasing penetration fraction. By comparison the NIF cryogenic capsule can tolerate a spike penetration depth of 29% for a half-yield of 7.5 MJ.[6]

VI. DOUBLE-SHELL DATABASE AND FUTURE DIRECTIONS

The fall-line figure-of-merit has played a prominent role in our exploration of robust double-shell ignition designs. An important question to address is the utility of this figure-of-merit applied to the Nova and Omega double-shell database as a check for consistency. As we noted in the Introduction the performance of double-shells to date has been promising and disappointing depending on the type of inner shell fielded. In Fig. 12 we show the neutronic YoC behavior of three generic types of double-shell that have been shot over the past two years on Omega versus fall-line parameter $\Delta\tau$. The range of measured neutron yields is 10^7-10^8 and calculated peak fuel ion temperatures are near 1 keV for all the indicated targets. An interesting correlation is seen between fall-line behavior and performance. The best performing targets had large (negative) $\Delta\tau$ while the underachieving targets had significantly positive $\Delta\tau$ without exception. This plot is intended only to demonstrate that the current Omega double-shell database is consistent with the fall-line design figure-of-merit $\Delta\tau$. Such a correlation provides some confidence in our fall-line design criterion that we have implemented in our ignition designs to date. We emphasize that the fall-line figure-of-merit is not a substitute for a predictive mix model which, at a minimum, must differentiate between low- and high-Z pushers mixing with DT, e.g., CH vs SiO_2 (inner shells). The success of the fall-line figure-of-merit to date does not contradict or invalidate other possible explanations for the (all) glass inner-shell target performance such as target fabrication irregularities and M-shell flux asymmetry. The M-shell hypothesis for target degradation has been previously proposed as a leading candidate for the historically low performance of the standard double-shell target.[13]

Given that M- and L-shell preheat asymmetry may be key to the success of indirectly-driven double-shell performance and that such a nonequilibrium effect is difficult to calculate, a prudent course is to consider experimental methods for *in situ* measurements of M-shell flux and asymmetry near the center of the hohlraum. We propose the following experimental setup using a double-shell target geometry to directly measure the properties of M-shell flux. A large low-Z outer shell is used to absorb almost all of the thermal x-ray flux while allowing over 80% of the 2–4 keV radiation to be transmitted to the inner-shell which consists of a glass microballoon overcoated with 25 μm of CH. The glass readily absorbs the transmitted x rays but its radial expansion is heavily tamped by the overlying CH layer. Thus, the glass is forced to expand inward and standard x-ray backlighting techniques[8] can directly track the trajectory of this M-shell-driven implosion. A large outer shell is chosen in order to delay the collision with the inner shell until the preheat-driven implosion has advanced sufficiently for diagnostic detection. We estimate that a 10% P_2 flux asymmetry in 2–4 keV radiation will translate into a nearly -10 μm P_2 distortion of the glass by the time of half-convergence. By tracking the trajectory of the imploding glass direct information on the level of M-shell flux and asymmetry can be obtained.

Beyond the effect of asymmetry, M-shell radiation can affect double-shell performance in another important respect. All of the high YoC targets shown in Fig. 12 are influenced to a considerable extent by volume absorption and heating of the inner-shell due to M-shell preheat. The inner-shell thus

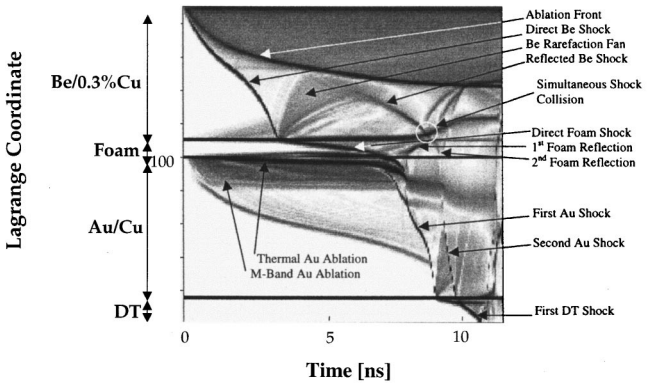

FIG. 13. The simulated logarithmic derivative of density versus time and Lagrange coordinate (integrated mass) for 250 eV 670 kJ double-shell design [Fig. 1(d)]. Shock- and ablation-front features are as indicated.

behaves as an exploding pusher to an appreciable degree, promoting early and robust neutron production at arrival of the first shock ($\approx$50%) at the expense of neutron production from the subsequent stagnation phase of the implosion. By contrast the standard (glass inner-shell) double-shells do not behave in this mode, producing the vast majority ($>$99.5%) of their yield during fuel stagnation and thereby assuming an increased risk of mix-induced degradation. The current challenge for the double-shell effort is to field an ''ignition-like'' target on Omega which emulates many (but obviously not all) of the properties of the ignition target described earlier while still giving good YoC behavior. Figure 13 displays many of the radiation-hydrodynamics aspects of the 250 eV ignition target in terms of shock- and ablation-front trajectories that could prove helpful in designing the next generation double-shell experiment on Omega. There are two important features in Fig. 13 that we wish to emphasize. First, there are two principal shocks that drive the implosion of the inner shell. Second, we note that the second shock originates at an intermediate time from a rarefaction fan reaching the ablation front and generating a steepening compression wave. This shock collides with a reflection shock originating from passage of the outer surface of the inner shell by the first shock. We have found that favorable fall-line behavior coincides well with the second shock collision occurring near the inner surface of the outer shell as indicated in Fig. 13. Thus, we refer to ignition-like behavior when the implosion is dominated by two principal shocks as just described with a relative timing such that the second shock collides with a reflected shock near the inner edge of the outer shell. To capture such ignition-like properties we propose that a variant of the pure CH double-shells successfully fielded on Omega be modified by doping the outer shell to reduce the M-shell preheat of the inner shell to acceptably low levels. Designs are in progress to optimize this scheme and to adapt standard core-imaging techniques, e.g., Ar-doping of the fuel, for direct diagnosis of double-shell implosion symmetry.

VII. SUMMARY

Using modern mix calculations, integrated hohlraum simulations and fall-line optimization we have begun to assess the viability of double-shell ignition on the NIF. Together these methods form the basis for our optimism that the prospects for achieving double-shell ignition have improved. The path to double-shell ignition will require a dedicated experimental commitment with the Omega laser to benchmark our understanding of mix and asymmetry. With regard to mix the calculations done to date reveal no adverse surprises, but in view of their phenomenological nature such predictions must be considered as tentative at best. Continuing experimental efforts aimed at constraining the relevant model parameters will likely lead to an improved predictive capability and a benefit for double-shell research. Rather than focusing on a particular mix model to validate a double-shell ignition design we have emphasized the fall-line figure-of-merit as a physically appealing tool for minimizing mix. Additional margin to mix may be required depending on the evolving status of modern mix calculations. For example, introduction of a low-Z mandrel on the inner surface of the high-Z inner shell might reduce the effects of mix in quenching fusion. Preliminary calculations using a 20 micron thick layer of Be inside the Au/Cu shell are promising and show unchanged fall-line behavior and no deterioration in clean yield with such a low-Z buffering layer. Simulations of double-shells using denser inner shell materials, e.g., a Pt/Ir alloy (80/20), also suggest improved performance by providing both higher clean yield and more fall-line delay.

ACKNOWLEDGMENTS

We are grateful to G. Dimonte, O. Jones, D. Rowley, and Alek Shestakov for useful discussions.

This work was performed under the auspices of the U.S. Department of Energy by the Lawrence Livermore National Laboratory under Contract No. W-7405-Eng-48.

[1] J. A. Paisner, J. D. Boyes, S. A. Kumpan, W. H. Lowdermilk, and M. S. Sorem, Laser Focus World **30**, 75 (1994).
[2] S. W. Haan, S. M. Pollaine, J. D. Lindl *et al.*, Phys. Plasmas **2**, 2480 (1995).
[3] J. K. Hoffer and L. R. Foreman, Phys. Rev. Lett. **60**, 1310 (1988); J. Sanchez and W. H. Giedt, Fusion Technol. **36**, 346 (1999).
[4] G. W. Collins, D. N. Bittner, E. Monsler, S. Letts, E. R. Mapoles, and T. P. Bernat, J. Vac. Sci. Technol. A **14**, 2897 (1996).
[5] J. Sater, B. Kozioziemski, G. W. Collins, E. R. Mapoles, and J. Pipes, Fusion Technol. **36**, 229 (1999).
[6] J. D. Lindl, *Inertial Confinement Fusion* (Springer-Verlag, New York, 1998).
[7] D. H. Munro, P. M. Celliers, G. W. Collins, D. M. Gold, L. B. DaSilva, S. W. Haan, R. C. Cauble, B. A. Hammel, and W. W. Hsing, Phys. Plasmas **8**, 2245 (2001).
[8] S. M. Pollaine, D. K. Bradley, O. L. Landen, R. J. Wallace, O. S. Jones, P. A. Amendt, L. J. Suter, and R. E. Turner, Phys. Plasmas **8**, 2357 (2001).
[9] L. J. Suter, J. Rothenberg, D. Munro, B. Van Wonterghem, and S. Haan, Phys. Plasmas **7**, 2092 (2000).
[10] T. R. Boehly, D. R. Brown, R. S. Craxton *et al.*, Opt. Commun. **133**, 495 (1997).
[11] S. A. Colgate and A. G. Petschek, ''Minimum conditions for the ignition of fusion,'' LA-UR-88-1268, 1988; copies may be obtained from the National Technical Information Service, Springfield, VA 22161.
[12] R. G. Watt, N. D. Delamater, P. L. Gobby, V. M. Gomez, J. E. Moore, G. D. Pollak, W. S. Varnum, and J. D. Colvin, Bull. Am. Phys. Soc. **44**, 166 (1999).

[13]W. S. Varnum, N. D. Delamater, S. C. Evans *et al.*, Phys. Rev. Lett. **81**, 5153 (2000).
[14]D. B. Harris and W. S. Varnum, Bull. Am. Phys. Soc. **41,** 1479 (1996).
[15]G. B. Zimmerman and W. L. Kruer, Comments Plasma Phys. Controlled Fusion **2**, 51 (1975).
[16]J. D. Ramshaw, Phys. Rev. E **58**, 5834 (1998).
[17]G. Dimonte and M. Schneider, Phys. Rev. E **54**, 3740 (1996); G. Dimonte, Phys. Plasmas **6**, 2009 (1999).
[18]P. Amendt, A. I. Shestakov, O. L. Landen, D. K. Bradley, S. M. Pollaine, L. J. Suter, and R. E. Turner, Phys. Plasmas **8**, 2908 (2001).
[19]L. V. Powers, R. L. Berger, R. L. Kauffman *et al.*, Phys. Plasmas **2**, 2473 (1995).
[20]E. A. Williams (private communication, 2000).
[21]R. E. Tipton, D. J. Steinberg, and Y. Tomita, Jpn. Soc. Mech. Eng. Int. J. Ser. II **35**, 67 (1992).
[22]D. L. Youngs, Physica D **12**, 32 (1984).
[23]C. G. Speziale, Annu. Rev. Fluid Mech. **23**, 107 (1991).
[24]J. D. Ramshaw, Phys. Rev. E **61**, 5339 (2000).